

# Tropospheric Dispersive Phase Anomalies during Heavy Rain Detected by L-band InSAR and Their Interpretation

Naufal Setiawan (✉ [naufal.setiawan89@gmail.com](mailto:naufal.setiawan89@gmail.com))

Hokkaido University: Hokkaido Daigaku <https://orcid.org/0000-0002-2350-4477>

Masato Furuya

Hokkaido University: Hokkaido Daigaku

---

## Full paper

**Keywords:** heavy rain, non-dispersive medium, dispersive medium, interferometric synthetic aperture radar, split-spectrum method.

**Posted Date:** June 22nd, 2021

**DOI:** <https://doi.org/10.21203/rs.3.rs-269140/v1>

**License:**  This work is licensed under a Creative Commons Attribution 4.0 International License.

[Read Full License](#)

---

**Version of Record:** A version of this preprint was published at Earth, Planets and Space on July 16th, 2021. See the published version at <https://doi.org/10.1186/s40623-021-01470-9>.

**Title page:**

Tropospheric Dispersive Phase Anomalies during Heavy Rain Detected by L-band InSAR  
and Their Interpretation

Author #1: Naufal Setiawan.\*

Department of Natural History Sciences, Graduate School of Science,  
Hokkaido University, Japan.

[naufal.setiawan89@gmail.com](mailto:naufal.setiawan89@gmail.com)

Author #2: Masato Furuya.

Department of Earth and Planetary Sciences, Faculty of Science, Hokkaido  
University, Japan.

[furuya@sci.hokudai.ac.jp](mailto:furuya@sci.hokudai.ac.jp)

\* corresponding author.

## **Abstract**

The split-spectrum method (SSM) can largely isolate and correct for the ionospheric contribution in the L-band interferometric synthetic aperture radar (InSAR). The standard SSM is performed on the assumption of only the first-order ionospheric dispersive effect, which is proportional to the total electron content (TEC). It is also known that during extreme atmospheric events, either originated from the ionosphere or in the troposphere, other dispersive effects do exist and potentially provide new insights into the dynamics of the atmosphere, but there have been few detection reports of such signals by InSAR. We apply L-band InSAR into heavy rain cases and examine the applicability and limitation of the standard SSM. Since no events such as earthquakes to cause surface deformation took place, the non-dispersive component is apparently attributable to the large amount of water vapor associated with heavy rain, whereas there are spotty anomalies in the dispersive component that are closely correlated with the heavy rain area. The ionosonde and Global Navigation Satellite System (GNSS) rate of total electron content index (ROTI) map both show little anomalies during the heavy rain, which suggests few ionospheric disturbances. Therefore, we interpret that the spotty anomalies in the dispersive component of the standard SSM during heavy rain are originated in the troposphere. While we can consider two physical mechanisms, one is runaway electron avalanche and the other is the dispersive effect due to rain, comparison with the observations from the ground-based lightning detection network and rain gauge data, we conclude that the rain dispersive effect is spatiotemporally favorable. We further propose a formulation to examine if another dispersive phase than the first-order TEC effect is present and apply it to the heavy rain

cases as well as two extreme ionospheric sporadic-E events. Our formulation successfully isolates the presence of another dispersive phase during heavy rain that is in positive correlation with the local rain rate. In comparison with other dispersive phases during Sporadic-E episodes, the dispersive heavy rain phases seem to have the same order of magnitude with the ionospheric higher-order effects.

**Keywords:** heavy rain, non-dispersive medium, dispersive medium, interferometric synthetic aperture radar, split-spectrum method.

## **1. Introduction**

InSAR is one of the space geodetic techniques that can map ground displacements with unprecedented spatial resolution without installing ground-based stations like GNSS, which is made possible by processing two images of Synthetic Aperture Radar (SAR) at the same area captured at different times (e.g., Hanssen, 2001). Both InSAR and GNSS, are based on phase measurement of the carrier microwaves, which experiences either a delay or advance, depending on the propagation media that are different than vacuum (e.g., Hanssen, 2001; Hobiger and Jakowski, 2017). The delay or advance is caused by the refractivity of the propagating medium, which is grouped into either dispersive or non-dispersive media. The refractivity in dispersive media depends on the carrier frequency of the microwave, and the ionosphere is the most significant dispersive medium for space geodesy and microwave remote sensing. On the other hand, the refractivity in the troposphere has been modeled as a function of air temperature, surface air pressure, and water vapor pressure (Thayer, 1974; Bevis et al., 1994) and is considered to be independent of the carrier frequency particularly in space geodetic techniques. Taking advantage of these differences between ionosphere

and troposphere, GNSS operationally utilizes dual-frequency observations not only to estimate the ionospheric TEC (e.g., Saito et al., 1998) but also to separate the water vapor content, thereby playing a role of atmospheric sensing tool as well (e.g., Bevis et al., 1994; Shoji, 2013).

Meanwhile, even in L-band InSAR, no operational dual-frequency analysis has been done until recently as it is based only on a single carrier-frequency observation. Therefore, several approaches have been proposed, such as range split-spectrum (Brcic et al., 2010; Rosen et al., 2010, Gomba et al., 2016), range phase group delay (Meyer et al., 2006), and multiple aperture interferometry and its along-track integration (Jung et al., 2013). One recently well-accepted technique is SSM that takes advantage of its finite bandwidth due to the linear frequency modulation in the original radar pulse (Brcic et al., 2010; Rosen et al., 2010, Gomba et al., 2016). To enhance the range resolution in SAR imageries, instead of transmitting a short and intense pulse, each radar pulse is frequency-modulated so that instantaneous frequency will change linearly over the pulse length (Curlander and McDonough, 1991; Hanssen, 2001); the wider the bandwidth in the frequency modulation, the better the range resolution. In the SSM, we split the original bandwidth in the range directly into high and low sub-bands and demodulates into the new higher and lower carrier frequencies (Brcic et al., 2010; Rosen et al., 2010, Gomba et al., 2016; Furuya et al., 2017). Thus, we can derive new InSAR images  $\Delta\phi_H$  and  $\Delta\phi_L$  and virtually perform dual-frequency InSAR observations, whereas the original range resolution is lost and the proximity of new frequencies might be a problem; the subscript  $H$  and  $L$  stand for higher

and lower carrier frequencies. Using the new InSAR images  $\Delta\phi_H$  and  $\Delta\phi_L$ , we can retrieve the dispersive and non-dispersive phase (Gomba et al., 2016);

$$\Delta\phi_{non-dispersive} = \frac{f_0}{(f_H^2 - f_L^2)} (\Delta\phi_H f_H - \Delta\phi_L f_L) \quad 1$$

$$\Delta\phi_{dispersive} = \frac{f_H f_L}{f_0 (f_H^2 - f_L^2)} (\Delta\phi_L f_H - \Delta\phi_H f_L)$$

where  $f_0$ ,  $f_H$ , and  $f_L$  are the original, new higher, and lower carrier frequency, respectively. As noted above, the  $\Delta\phi_{dispersive}$  is the contribution of the phase advance due to TEC in the ionosphere, whereas the  $\Delta\phi_{non-dispersive}$  includes the effects due to surface deformation and tropospheric delay after a removal of orbital and topographic phases.

The above formula is developed based on the dispersive nature of the ionosphere that follows the Appleton-Hartree equation (Belcher., 2008). Yet, it only accounts for the first-order term in the refractive index that is proportional to the ionospheric TEC and inversely proportional to the frequency-squared, since the higher-order terms of the ionosphere is assumed to be negligible as follows:

$$n = 1 - 40.3 TEC / f^2 \quad 2$$

However, if extreme ionospheric events occurred, such as Sporadic-E, we may have to consider higher-order ionosphere effects as have been considered in GNSS (Kedar et al., 2003) and InSAR (Furuya et al., 2017).

Although no tropospheric dispersive effects are included in eq. (2), which is generally a good approximation, the refractive index of the troposphere can also depend on the frequency and even become complex (e.g., Van de Hulst., 1957; Crane., 1967; Zufferey. 1972; Liebe, 1989; Solheim et al., 1999); we assume that the contributions to the imaginary

part of refractive index are negligible in L-band. Even though the effect of molecular resonances is negligible for L-band because of its far location from the resonant frequencies, the dispersive effect is caused by forward scattering from nongaseous larger particles (> 1mm in size) such as rain droplet, hail and snow (Solheim et al., 1999). Based on the transition matrix approach for computing scattering properties (Oguchi, 1983), Solheim et al (1999) showed that L1 microwave propagation through 1-km of heavy rain could cause 15 mm of delay. To our knowledge, however, no observational verifications have been done on the theoretical prediction, using the real GNSS data during heavy rain. In addition to the forward scattering mechanism from rain droplet, we may conceive another possible mechanism for tropospheric dispersive phase, motivated by the recent development of High-Energy Atmospheric Physics (e.g., Dwyer et al., 2012). It is now well-established that high-energy particles such as X-ray and Gamma-ray are radiated in association with thunderclouds and lightning initiation and detected either in situ by aircraft (Kelley et al., 2015) or on the ground (Wada et al., 2018). Those X-ray or Gamma-ray emissions are thought to be caused by bremsstrahlung of the relativistic runaway electron avalanches that are accelerated under the electric field in the troposphere (Gurevich et al., 1992; Dwyer, 2003; Gurevich et al., 2004). Troposphere can thus become natural accelerator and contain accelerated electrons that are, if ever, local and transient, while it is unclear if such electrons could become comparable to the background TEC.

In this study, we first apply the standard SSM to InSAR images acquired during heavy rain (rainfall rate exceeding 50 mm/hour) in Japan, so that we can confirm the presence of both huge amount of water vapor in the  $\Delta\phi_{non-dispersive}$  and a long-wave trend due to the

ionospheric TEC in the  $\Delta\phi_{dispersive}$ ; we confirmed no surface deformation episodes such as earthquakes. In addition to those expected phase anomalies, however, there are spotty anomalies in the  $\Delta\phi_{dispersive}$  of the SSM which are clearly neither identical to the long-wavelength ionospheric phase, nor, to the localized strong anomalies due to the Sporadic-E (Furuya et al., 2017).

Then, following two previous physical mechanisms during heavy rain, we examine the spotty anomalies in the  $\Delta\phi_{dispersive}$  of the SSM with the ground-based ionosonde, GNSS TEC map, lightning detection network, and rain gauge data. Furthermore, we propose a formulation to examine the presence of another dispersive phase and apply it to heavy rain cases. We attempt to quantify the magnitude of another dispersive phase with rain rate from the weather data by calculating the root mean square (RMS) value. We also test our proposed equation on other extreme atmospheric phenomena that originated in the ionosphere, the Sporadic-E.

## **2. Anomaly observed in $\Delta\phi_{dispersive}$ of SSM during heavy rain**

### *2.1. Data and processing strategy*

Heavy rain occurrences are detectable using the Japan Meteorological Agency (JMA) weather radar observation network that consists of 20 rain radar antennas in the whole Japan island and delivers rain rate every 10 minutes over Japan with a spatial resolution of ~1km (<http://database.rish.kyoto-u.ac.jp/arch/jmadata/data/jma-radar/synthetic/original/>). Then, we look for the data availability for L-band ALOS-2/PALSAR-2 SM-1 mode images; the chirp bandwidth in the SM-1 mode is 79.4MHz. Under the basic observation

scenario of ALOS-2/PALSAR-2 over Japanese island, even the shortest recurrent interval for InSAR is 56 days, and thus there are limited opportunities for us to examine the impact of heavy rain in InSAR. Here we report two heavy rain cases in southern Japan, Kyushu on July 31, 2018 (Figure 1a) and Shikoku on August 15, 2018 (Figure 1b), respectively. We have confirmed that the other imaging dates were not affected by rain, by generating two other InSAR images for both Kyushu and Shikoku frames (Figures S1).

For InSAR processing, we use a commercial software package provided by Gamma remote sensing (Wegmueller et al., 1997). We utilize a 10 m digital elevation model (DEM) from the Geospatial Information Authority of Japan (GSI) to remove the topographic phase. We use the minimum cost flow algorithm for phase unwrapping (Constantini, 1998). During InSAR processing, we apply multi-looking (spatial averaging) 21 looks in range and 28 looks in azimuth for Kyushu, and 24 looks in range and 32 looks in azimuth for Shikoku, which results in the spatial resolutions of ~30m for Kyushu and ~34m for Shikoku in range and ~52m for Kyushu and ~68m for Shikoku in azimuth, respectively.

We utilize symmetric SSM to create new sub-bands, each new sub-band with one fifth of the original bandwidth. We create two new sub-band interferograms using the SSM processing strategy similar to Furuya et al. (2017); the details of ALOS-2/PALSAR-2 datasets for both InSAR and SSM processing are shown in Table 1. We employ total multi-looking with 60 looks in range and 88 looks in azimuth for Kyushu, and 93 looks in range and 124 looks in azimuth for Shikoku to accommodate coarser range resolution derived from the new narrower bandwidth. We do not apply the linear or quadratic plane fitting to mitigate the long-wavelength phase trend to preserve our geophysical interpretation.

## 2.2. InSAR and SSM result

InSAR heavy rain image of Kyushu shows, in addition to the broad anomaly to the northern edge, three localized anomalies in the middle of the images, each of which increase toward the center and reach 12 cm along satellite LOS direction (Figure 2a). Meanwhile, InSAR heavy rain image of Shikoku display an anomaly located near the eastern edge, reaching 16 cm along satellite LOS direction besides the broad anomalies in the south-west (Figure 2b). Additionally, the coherence map of both InSAR heavy rain images shows a good result (Figure S2). There is no large surface deformation associated with an earthquake between those acquisition dates of InSAR heavy rain images in Kyushu and Shikoku according to the JMA earthquake catalog.

We do not identify any similar anomalies in fair-weather pairs (Figure S3). As demonstrated previously by InSAR image during rainy conditions, for instance, from the C-band ERS tandem satellite (Hanssen et al., 1999) and L-band ALOS/ PALSAR satellite (Kinoshita et al., 2013), these localized anomalies are presumably due to a large water vapor during heavy rain. Next, we apply the SSM to confirm the occurrence of water vapor in the InSAR images in the  $\Delta\phi_{non-dispersive}$ , since the water vapor is a non-dispersive medium by definition.

As we set the bandwidth of the SSM to be one-fifth of the original bandwidth, the range resolution is five-times coarser, resulting in noisier images. However, the total multi-looking described in the previous sub-section can reduce the increased speckle noise, and the InSAR images with new frequencies (Figures S4, S5) are quite analogous to the original InSAR images in Figures 2 and S3.

The results of the  $\Delta\phi_{non-dispersive}$  in Figures 3a and 4a confirm the presence of huge water vapor during heavy rain. However, the  $\Delta\phi_{dispersive}$  in Figures 3b and 4b in heavy rain pairs show spotty anomalies aside from the long-wavelength trend induced by the first-order effect of the ionosphere; we confirm the absence of any anomalies both in non-dispersive and dispersive phases in fair weathers (Figure S7).

### **3. Origin of the $\Delta\phi_{dispersive}$ spotty anomalies of SSM**

To examine if there were any anomalies in the ionosphere, we check the GNSS ROTI (<https://aer-nc-web.nict.go.jp/GPS/GEONET/RMAP/>) and the ionosonde data ([https://wdc.nict.go.jp/ionog/js\\_viewer/js\\_02.html](https://wdc.nict.go.jp/ionog/js_viewer/js_02.html)) from the National Institute of Communication Technologies of Japan (NICT). They do not show any anomalies during the heavy rain events, which suggests a steady ionosphere during the SAR acquisitions. We examine the two possible mechanisms originated in the troposphere, by comparing the  $\Delta\phi_{dispersive}$  of SSM with ground-based lightning detection network and rain gauge data. Firstly, we try to associate the spotty signal in the  $\Delta\phi_{dispersive}$  of SSM with the runaway electron avalanche during lightning initiation and thundercloud. To confirm our interpretation, we collect lightning data from Japan Lightning Detection Network (JLDN), which tells their location, incident time, electric current, thunder or cloud discharge. The collected lightning data cover about 30 minutes before and after the scene centre observation time of SAR data.

In the Kyushu case on 31 July 2018, there is only one lightning occurred ~ 17 minutes after SAR observation time, but this lightning occurred outside the SAR observation scene

(Figures 5a, c). Meanwhile, in the Shikoku data, there occurred a number of lightning, but their occurrences and SAR imaging time are significantly distant, reaching ~15 minutes at maximum (Figures 6a, b). Furthermore, the lightning locations and the unknown spotty signal in the dispersive phase are not matching with each other (Figure 6a); the lightning clearly occurred on the western side of the spotty signals in  $\Delta\phi_{dispersive}$ .

Next, we compare the  $\Delta\phi_{dispersive}$  with the available rain gauge data derived from AMeDAS, Japanese nationwide ground-based weather observing system, which are distributed with ~17km interval and records local rain rate every 10 minutes. Figures 5d and 7b show higher rain rate around the SAR imaging time. In particular, the AMeDAS station 74391 located by chance inside the Shikoku heavy rain clearly demonstrates a very high rate by more than ~70 mm/hour at the time of SAR imaging, supporting that the high rain rate is a likely source for the spotty anomaly in the  $\Delta\phi_{dispersive}$ .

The comparison of  $\Delta\phi_{dispersive}$  spotty anomalies with the ground-based lightning detection network and rain gauge data show that the latter rain rate data gives higher correlation in terms of the spatial and temporal matching. We thus prefer an interpretation of the detection of forward scattering by rain droplet to the detection of runaway electron avalanche. However, in contrast to the terrestrial gamma-ray flash that will last only several milliseconds at the time of lightning discharge, another type of gamma-ray emission called “gamma-ray glow” is also known, which can last for several minutes and are not generally accompanied with lightning but are associated with thunderclouds (Wada et al., 2018). We thus consider that few correlations do not necessarily preclude the interpretation of runaway electron avalanche, whereas quantitative assessment of electron content is also necessary.

#### 4. Presence of another $\Delta\phi_{dispersive}$ during heavy rain

##### 4.1. Formulation to detect another dispersive phase

Given the spotty anomalies in the  $\Delta\phi_{dispersive}$  of heavy rain InSAR that presumably originates in the troposphere, we formulate the presence of another dispersive source aside from the first-order free electrons in the ionosphere. Since the SSM only account for phase advance due to the TEC, it is conceivable to add the presence of another dispersive effect in addition to the first order of the ionospheric effect. The new sub-band InSAR images,  $\Delta\phi_H$  and  $\Delta\phi_L$  will have  $\Delta\phi_{another\_disp}$ , aside from the  $\Delta\phi_{non-dispersive}$  and the  $\Delta\phi_{dispersive}$ . Unlike the conventional  $\Delta\phi_{non-dispersive}$  and the  $\Delta\phi_{dispersive}$  terms, however, no explicit expression for its frequency dependence is available, and we thus set it to be  $X(f)$  for convenience. To solve the three unknown phases, we need one additional observation, and thus, create the third sub-band InSAR. For simplicity, we use the original center frequency  $\Delta\phi_0$  with the same reduced bandwidth as  $\Delta\phi_H$  and  $\Delta\phi_L$ .

$$\begin{aligned}\Delta\phi_H &= \Delta\phi_{non-dispersive} \frac{f_H}{f_0} + \Delta\phi_{dispersive} \frac{f_0}{f_H} + \Delta\phi_{another\_disp} X(f_H) \\ \Delta\phi_L &= \Delta\phi_{non-dispersive} \frac{f_L}{f_0} + \Delta\phi_{dispersive} \frac{f_0}{f_L} + \Delta\phi_{another\_disp} X(f_L) \\ \Delta\phi_0 &= \Delta\phi_{non-dispersive} \frac{f_0}{f_0} + \Delta\phi_{dispersive} \frac{f_0}{f_0} + \Delta\phi_{another\_disp} X(f_0)\end{aligned}\quad 3$$

Then, to eliminate the  $\Delta\phi_{non-dispersive}$ , we divide each new InSAR sub-band images with each center frequency, followed by subtractions between  $\frac{\Delta\phi_H}{f_H}$  and  $\frac{\Delta\phi_L}{f_L}$ , and between  $\frac{\Delta\phi_0}{f_0}$  and  $\frac{\Delta\phi_L}{f_L}$ , we get the following;

$$\frac{\Delta\phi_H}{f_H} - \frac{\Delta\phi_L}{f_L} = \Delta\phi_{dispersive} \left( \frac{f_0}{f_H^2} - \frac{f_0}{f_L^2} \right) + \Delta\phi_{another\_disp} [X(f_H)/f_H - X(f_L)/f_L] \quad 4$$

$$\frac{\Delta\phi_0}{f_0} - \frac{\Delta\phi_L}{f_L} = \Delta\phi_{dispersive} \left( \frac{f_0}{f_0^2} - \frac{f_0}{f_L^2} \right) + \Delta\phi_{another\_disp} [X(f_0)/f_0 - X(f_L)/f_L] \quad 5$$

Further, we divide equations 4 and 5 with  $\left(\frac{1}{f_H^2} - \frac{1}{f_L^2}\right)$  and  $\left(\frac{1}{f_0^2} - \frac{1}{f_L^2}\right)$ , respectively, to obtain

the following equations,

$$\frac{\frac{\Delta\phi_H}{f_H} - \frac{\Delta\phi_L}{f_L}}{\left(\frac{1}{f_H^2} - \frac{1}{f_L^2}\right)} = \Delta\phi_{dispersive} f_0 + \frac{\Delta\phi_{another\_disp} [X(f_H)/f_H - X(f_L)/f_L]}{\left(\frac{1}{f_H^2} - \frac{1}{f_L^2}\right)} \equiv \Gamma(\Delta f) \quad 6$$

$$\frac{\frac{\Delta\phi_0}{f_0} - \frac{\Delta\phi_L}{f_L}}{\left(\frac{1}{f_0^2} - \frac{1}{f_L^2}\right)} = \Delta\phi_{dispersive} f_0 + \frac{\Delta\phi_{another\_disp} [X(f_0)/f_0 - X(f_L)/f_L]}{\left(\frac{1}{f_0^2} - \frac{1}{f_L^2}\right)} \equiv \Gamma(\Delta f)' \quad 7$$

We call this function  $\Gamma(\Delta f)$  and  $\Gamma(\Delta f)'$ , which consist of the  $\Delta\phi_{dispersive}$  and the

$\Delta\phi_{another\_disp}$ . Subtracting equation 7 from 6 to eliminate  $\Delta\phi_{dispersive} f_0$ , we can solve for

$\Delta\phi_{another\_disp}$  as follows;

$$\Delta\phi_{another\_disp} = [\Gamma(\Delta f) - \Gamma(\Delta f)'] / [Y(f_H) - Y(f_0)] \quad 8$$

where we replaced the  $\frac{[X(f_H)/f_H - X(f_L)/f_L]}{\left(\frac{1}{f_H^2} - \frac{1}{f_L^2}\right)}$  and the  $\frac{[X(f_0)/f_0 - X(f_L)/f_L]}{\left(\frac{1}{f_0^2} - \frac{1}{f_L^2}\right)}$  with  $[Y(f_H) - Y(f_L)]$

and  $[Y(f_0) - Y(f_L)]$ , respectively, for easier notation. In reality, however, the explicit

forms of  $X(f)$  and  $Y(f)$  are uncertain. To derive  $\Delta\phi_{another\_disp}$  consistently with the radian

unit, we simply divide the difference,  $\Gamma(\Delta f) - \Gamma(\Delta f)'$ , by  $10^9$  Hz so that we can evaluate

the magnitude of  $\Delta\phi_{another\_disp}$ .

#### 4.2. Results in heavy rain and fair-weather cases

First, we create the other ( $\Delta\phi_0$ ) sub-band images for both heavy rain and fair-weather in Kyushu and Shikoku; we now do not have to shift the center frequency but set the same bandwidth as the other sub-band images. The new images (Figure S6) are quite similar to the original InSAR images (Figures 2, S2), as well as the previous sub-band SSM images (Figures S3, S4).

The  $\Delta\phi_{another\_disp}$  estimated for both heavy rain and fair-weather cases are shown in Figures 8. We can clearly observe some spatial phase changes in the heavy rain image, (Figures 8a, c), whereas there are no significant spatial variations in the fair-weather image (Figures 8b, d). Moreover, compared with the original dispersive phases in Figures 3b and 4b, we should note that long-wavelength phases are significantly reduced in Figures 8a and 8c, suggesting that ionospheric first-order TEC effect could be successfully removed.

#### 4.3. Comparison of another dispersive phase with weather radar

In order to check if another dispersive phase is related with the local rain rate, we compare the  $\Delta\phi_{another\_disp}$  in Figures 8a and 8c with various rain rate ranges from the JMA weather radar; the distribution of AMeDAS rain gauge data is too sparse (~17km) to compare the InSAR data. We first categorized the rain captured by JMA weather radar into six and seven rain rate categories for Kyushu and Shikoku, respectively (Figure 9). Then, we compute the RMS of the  $\Delta\phi_{another\_disp}$  at the corresponding rain rate ranges, by selecting a point in weather radar and averaging  $\Delta\phi_{another\_disp}$  value in weather radar point vicinity. In both Kyushu (Figure 10a) and Shikoku (Figure 10c), the RMS values are largely in increasing trend with the rain rate in light of the 95 % confidence intervals, suggesting their

positive correlations between them; the large uncertainties at the very high rain rate are due to the small number of sample pixels. As a comparison, we also calculate the RMS of  $\Delta\phi_{non-dispersive}$ . In both Kyushu (Figure 10b) and Shikoku (Figure 10d), the RMS of  $\Delta\phi_{non-dispersive}$  has larger uncertainties than those in  $\Delta\phi_{another\_disp}$ , and there is no clear positive correlation with the rain rate. These contrasting results may verify that the tropospheric dispersive phases,  $\Delta\phi_{another\_disp}$ , are directly related to the rain rate. As the  $\Delta\phi_{non-dispersive}$  is physically attributed to the water vapor amount, instead of rain itself, the larger uncertainties in  $\Delta\phi_{non-dispersive}$  as well as no positive correlation with rain rate are reasonable.

However, the RMS values in the  $\Delta\phi_{another\_disp}$  are significantly different between the two locations. This would be because the  $\Delta\phi_{another\_disp}$  is simply derived by dividing  $\Gamma(\Delta f) - \Gamma(\Delta f)'$  with  $10^9$  Hz to compare its magnitude with other terms but still includes additional unknown factors that depend not only frequency but also other parameters such as the canting angle of rain drop, local wind direction and so on. In other words, we admit that theoretical modeling to physically relate any meteorological data to tropospheric dispersive phase is still in its infancy, which well deserves further studies.

#### *4.4. Confirmation of the higher-order ionospheric effect*

In order to quantitatively confirm the magnitude of another dispersive phase term, we further compute the  $\Delta\phi_{another\_disp}$  for the Sporadic-E events reported by Furuya et al. (2017) and compare with the heavy rain cases. Furuya et al (2017) performed minimum-norm inversion to suggest the presence of higher-order ionospheric effects without

generating the third sub-band InSAR images. In contrast, we have performed triple-frequency measurement by invoking  $\Gamma(\Delta f)'$  in addition to  $\Gamma(\Delta f)$  to eliminate both non-dispersive and first order TEC effect. Shown in Figure 11 is the existence of  $\Delta\phi_{another\_disp}$ , which shows the need to account for the higher order ionospheric effect during the Sporadic-E events. Moreover, looking at the  $\Delta\phi_{another\_disp}$  from both of heavy rain cases (Figures 8a, c) and Sporadic-E (Figure 11), we may conclude that the tropospheric dispersive phase in heavy rain seems to have the similar order of magnitude in comparison to the higher dispersive phase in the ionosphere during Sporadic-E events.

## Conclusion

We generated InSAR images that captured two heavy rain episodes in Japan and calculated the  $\Delta\phi_{non-dispersive}$  and  $\Delta\phi_{dispersive}$  using the SSM. While the  $\Delta\phi_{non-dispersive}$  is dominated presumably by the large water vapor signals, there are spotty anomalies in the  $\Delta\phi_{dispersive}$  in the rainy area. We proposed two distinct physical mechanisms and examined them with ground-based lightning observation and rain gauge data. As a result, the rain scattering dispersive effect is spatiotemporally more preferable to the runaway electron avalanche, demonstrating the possibility of simultaneous observation of rain droplet and water vapor with a single instrument at the same high spatial resolution. Based on a formulation to include another dispersive effect, we confirmed that another dispersive effect does exist during heavy rain but is absent in fair weather. Additionally, the  $\Delta\phi_{another-dispersive}$  originated probably from rain-droplet show a positive correlation with rain radar data, whereas the water-vapor driven  $\Delta\phi_{non-dispersive}$  does not. Another

dispersive phase associated with heavy rain is likely to have the same order of magnitude to the higher-order ionospheric effect during sporadic-E.

### **List of abbreviations**

AMeDAS: automated meteorological data acquisition system; ALOS-2: advanced land observation satellite-2; DEM: digital elevation model; GNSS: Global Navigation Satellite System; GSI: Geospatial Information Authority of Japan; InSAR: interferometric synthetic aperture radar; JLDN: Japan Lightning Detection Network; JMA: Japan Meteorological Agency; LOS: line of sight; MCF: minimum cost flow; NICT: National Institute of Communications and Technology of Japan; PALSAR-2: phased array L-band synthetic aperture radar-2; RMS: root mean square; ROTI: rate of total electron content index; SAR: synthetic aperture radar; SM-1: strip map mode -1; SSM: split-spectrum method; TEC: total electron content.

### **Authors' contribution**

MF conceptualize the research and supervise during the research. NS search and process heavy rain cases. Both of the authors write, read, and approve the final manuscript.

### **Availability of data and materials**

The ALOS-2/PALSAR-2 level 1.1 used in this study available upon purchase through RESTEC (<https://www.restec.or.jp/en/>) or PASCO (<http://en.alos-pasco.com>). We can share the data upon request within a framework of collaboration with our research group. We used the GAMMA (<https://www.gamma-rs.ch>), and MATLAB for processing. The weather radar and AMeDAS data are accessible and the courtesy of the Japan

Meteorological Agency. The weather data also accessible from (<http://database.rish.kyoto-u.ac.jp/arch/jmadata/data/jma-radar/synthetic/original/>) maintained by RISH, Kyoto University. The lightning data available upon purchase from Franklin Japan (<https://www.franklinjapan.jp/>).

### **Acknowledgements**

The ALOS-2/ PALSAR-2 level 1.1 data in this study are shared among PIXEL (PALSAR Interferometry Consortium to Study our Evolving Land Surface) under a cooperative research contract with the Earthquake Research Institute, University of Tokyo. The ownership of ALOS-2/PALSAR-2 data belongs to JAXA. The ownership of weather radar and AMeDAS data belongs to the JMA. We acknowledge two anonymous reviewers and an editor whose comments were helpful to revise the original manuscript.

### **Competing interests**

The authors declare that they have no competing interests.

### **Ethics approval and consent to participate**

Not applicable.

### **Funding**

NS is grateful to JICA Innovative Asia for financially supporting his master's study at Hokkaido University. This study also partially supported by Specific Research Project (B), "Study on the crustal and surface deformation using multiple SAR techniques, at Earthquake Research Institute, the University of Tokyo.

## References

- Belcher DP (2008) Theoretical Limits on SAR Imposed by the Ionosphere. IET Radar, Sonar and Navigation, vol. 2, no. 6, pp. 435–448. <https://doi.org/10.1049/iet-rsn:20070188>
- Bevis M, Businger S, Chiswell S, Herring TA, Anthes RA, Rocken C, Ware RH (1994) GPS Meteorology: Mapping Zenith Wet Delays onto Precipitable Water. Journal of Applied Meteorology, vol. 33, no. 3, 1994, pp. 379–386. [https://doi.org/10.1175/1520-0450\(1994\)033<0379:gmmzwd>2.0.co;2](https://doi.org/10.1175/1520-0450(1994)033<0379:gmmzwd>2.0.co;2)
- Brcic R, Parizzi A, Eineder M, Bamler R, Meyer F (2010) Estimation and Compensation of Ionospheric Delay for SAR Interferometry. IEEE International Geoscience and Remote Sensing Symposium, 2010. <https://doi.org/10.1109/igarss.2010.5652231>
- Costantini M (1998) A Novel Phase Unwrapping Method Based on Network Programming. IEEE Transactions on Geoscience and Remote Sensing 36, no. 3: 813–21. <https://doi.org/10.1109/36.673674>
- Crane RK (1967) Coherent Pulse Transmission through Rain. IEEE Transactions on Antennas and Propagation, vol. 15, no. 2, 1967, pp. 252–256. <https://doi.org/10.1109/tap.1967.1138897>
- Curlander JC, McDonough RN (1991) Synthetic Aperture Radar: Systems and Signal Processing. J. Wiley
- Dwyer JR (2003) A fundamental limit on electric fields in air. Geophys. Res. Lett., 30, 2055. <https://doi.org/10.1029/2003GL017781>

Dwyer JR, Smith DM, Cummer SA (2012) High-Energy Atmospheric Physics: Terrestrial Gamma-Ray Flashes and Related Phenomena. *Space Science Reviews* 173, no. 1-4: 133–96. <https://doi.org/10.1007/s11214-012-9894-0>

Furuya M, Suzuki T, Maeda J, Heki K (2017) Midlatitude Sporadic-E Episodes Viewed by L-Band Split-Spectrum InSAR. *Earth, Planets and Space* 69, no. 1. <https://doi.org/10.1186/s40623-017-0764-6>

Gomba G, Parizzi A, Zan FD, Eineder M, Bamler R (2016) Toward Operational Compensation of Ionospheric Effects in SAR Interferograms: The Split-Spectrum Method. *IEEE Transactions on Geoscience and Remote Sensing* 54, no. 3: 1446–61. <https://doi.org/10.1109/tgrs.2015.2481079>

Gurevich AV, Milikh GM, Roussel-Dupre R (1992) Runaway Electron Mechanism of Air Breakdown and Preconditioning during a Thunderstorm. *Physics Letters A* 165, no. 5-6: 463–68. [https://doi.org/10.1016/0375-9601\(92\)90348-p](https://doi.org/10.1016/0375-9601(92)90348-p)

Gurevich AV, Medvedev YV, Zybin KP (2004) New Type Discharge Generated in Thunderclouds by Joint Action of Runaway Breakdown and Extensive Atmospheric Shower. *Physics Letters A*, vol. 329, no. 4-5, pp. 348–361, <https://doi.org/10.1016/j.physleta.2004.06.099>

Hanssen RF, Weckwerth TM, Zebker HA, Klees R (1999) High-Resolution Water Vapor Mapping from Interferometric Radar Measurements. *Science* 283, no. 5406: 1297–99. <https://doi.org/10.1126/science.283.5406.1297>

Hanssen RF (2001) *Radar Interferometry: Data Interpretation and Error Analysis*. Kluwer Academic Publishing

Hobiger T, Jakowski N (2017) Atmospheric Signal Propagation. Springer Handbook of Global Navigation Satellite Systems, by Peter J. G. Teunissen and Oliver Montenbruck, Springer., pp. 165–193

Hulst HC (1957) Light Scattering by Small Particles. Wiley

Jung HS, Lee DT, Lu Z, Wong JS (2013) Ionospheric Correction of SAR Interferograms by Multiple-Aperture Interferometry. IEEE Transactions on Geoscience and Remote Sensing, vol. 51, no. 5, pp. 3191–3199. <https://doi.org/10.1109/tgrs.2012.2218660>

Kedar S, Hajj GA, Wilson BD, Heflin MB (2003) The Effect of the Second Order GPS Ionospheric Correction on Receiver Positions. Geophysical Research Letters, vol. 30, no. 16, <https://doi.org/10.1029/2003gl017639>

Kelley NA, Smith DM, Dwyer JR, Splitt M, Lazarus S, Martinez-Mckinney F, Hazelton B, Grefenstette B, Lowell A, Rassoul HK (2015) Relativistic Electron Avalanches as a Thunderstorm Discharge Competing with Lightning. Nature Communications, vol. 6, no. 1, <https://doi.org/10.1038/ncomms8845>

Kinoshita Y, Shimada M, Furuya M (2013) InSAR Observation and Numerical Modeling of the Water Vapor Signal during a Heavy Rain: A Case Study of the 2008 Seino Event, Central Japan. Geophysical Research Letters 40, no. 17: 4740–44. <https://doi.org/10.1002/grl.50891>

Liebe HJ (1989) MPM-An atmospheric millimeter-wave propagation model. Int J Infrared Milli Waves 10, 631–650. <https://doi.org/10.1007/BF01009565>

Meyer F, Bamler R, Jakowski N (2006) The Potential of Low-Frequency SAR Systems for Mapping Ionospheric TEC Distributions. *IEEE Geoscience and Remote Sensing Letters*, vol. 3, no. 4, pp. 560–564. <https://doi.org/10.1109/lgrs.2006.882148>

Oguchi T (1983) Electromagnetic Wave Propagation and Scattering in Rain and Other Hydrometeors, *Proc. IEEE*, 71(9), 1029-1078, <https://doi.org/10.1109/PROC.1983.12724>

Rosen PA, Hensley S, and Chen C (2010) Measurement and Mitigation of the Ionosphere in L-Band Interferometric SAR Data. 2010 IEEE Radar Conference, <https://doi.org/10.1109/radar.2010.5494385>

Saito A, Fukao S, Miyazaki S (1998) High Resolution Mapping of TEC Perturbations with the GSI GPS Network over Japan. *Geophysical Research Letters*, vol. 25, no. 16, 1998, pp. 3079–3082. <https://doi.org/10.1029/98gl52361>

Shoji Y (2013) Retrieval of Water Vapor Inhomogeneity Using the Japanese Nationwide GPS Array and Its Potential for Prediction of Convective Precipitation. *Journal of the Meteorological Society of Japan. Ser. II*, vol. 91, no. 1, pp. 43–62., <https://doi.org/10.2151/jmsj.2013-103>

Solheim FS, Vivekanandan J, Ware RH, and Rocken C (1999) Propagation Delays Induced in GPS Signals by Dry Air, Water Vapor, Hydrometeors, and Other Particulates. *Journal of Geophysical Research: Atmospheres* 104, no. D8: 9663–70. <https://doi.org/10.1029/1999jd900095>

Thayer GD (1974) An Improved Equation for the Radio Refractive Index of Air. *Radio Science*, vol. 9, no. 10, pp. 803–807. <https://doi.org/10.1029/rs009i010p00803>

Wada, Y, Bowers GS, Enoto T, Kamogawa M, Nakamura Y, Morimoto T, Smith DM, Furuta Y, Nakazawa K, Yuasa T, Matsuki A, Kubo M, Tamagawa T, Makishima K, Tsuchiya H (2018) Termination of Electron Acceleration in Thundercloud by Intracloud/Intercloud Discharge. *Geophysical Research Letters*, vol. 45, no. 11, pp. 5700–5707. <https://doi.org/doi:10.1029/2018gl077784>

Wegmüller U, Werner CL (1997) GAMMA SAR processor and interferometry Software, Proceedings 3rd ERS Scientific Symposium, Florence, Italy, 17-20 March 1997.

Wessel P, Luis JF, Uieda L, Scharroo R, Wobbe F, Smith WHF, Tian D (2019) The Generic Mapping Tools version 6. *Geochemistry, Geophysics, Geosystems*, 20, 5556–5564. <https://doi.org/10.1029/2019GC008515>

Zufferey CH (1972) A Study of Rain Effects on Electromagnetic Waves in the 1-600 Ghz Range. University of Colorado

### **Figures legend**

Figure 1. JMA weather radar observation on; (a) Kyushu at 20180731\_1520UTC and (b) Shikoku at 20180815\_0310UTC; we use a convention YYYYMMDD to denote the imaging year, month and date. Orange square denotes the SAR imaging area taken by ALOS-2/PALSAR-2 SM-1 mode.

Figure 2. Original bandwidth differential interferogram of heavy rain pairs; (a) Kyushu on 20180731\_20180828, and (b) Shikoku 20180815\_20181107.

Figure 3. The retrieval of standard SSM on Kyushu 20180731\_20180828; (a)  $\Delta\phi_{non-dispersive}$ , and (b)  $\Delta\phi_{dispersive}$ .

Figure 4. The retrieval of standard SSM on Shikoku 20180815\_20181107; (a)

$\Delta\phi_{non-dispersive}$ , and (b)  $\Delta\phi_{dispersive}$ .

Figure 5. The  $\Delta\phi_{dispersive}$  of SSM on Kyushu 20180731\_20180828; (a) overlaid by lightning location and (b) overlaid by the AMeDAS station distribution. The temporal relations of (c) the lightning, (d) ten minutes rainfall with the SAR observation time that is indicated with the black dashed line.

Figure 6. The  $\Delta\phi_{dispersive}$  of SSM on Shikoku 20180815\_20181107. (a) Overlaid by lightning location with an expanded view near the lightening (b) Temporal relation of the lightning with the SAR imaging time indicated with the black dashed line.

Figure 7. The  $\Delta\phi_{dispersive}$  of SSM on Shikoku 20180815\_20181107. (a) Overlaid by the AMeDAS station distribution and (b) the temporal changes in the ten minutes rainfall and the SAR imaging time indicated with the black dashed line.

Figure 8. The  $\Delta\phi_{another\_disp}$  derived from triple-frequency SSM (a) Kyushu 20180731\_20180828 with heavy rain, (b) Kyushu 20180410\_20180828 without heavy rain, (c) Shikoku 20180815\_20181107 with heavy rain, (d) Shikoku 20180228\_20181107 without heavy rain.

Figure 9. Rain rate ranges over (a) Kyushu on 20180731 at 1520UTC and (b) Shikoku on 20180815 at 0310UTC. Orange squares denote the SAR imaging area taken by ALOS-2/PALSAR-2 SM-1 mode. Colors indicate rain rate in mm/hour.

Figure 10. RMS plot of  $\Delta\phi_{another\_disp}$  for. (a) Kyushu 20180731\_20180828, (c) Shikoku 20180815\_20181107. RMS plot of  $\Delta\phi_{non-dispersive}$  for (b) Kyushu 20180731\_20180828, (d) Shikoku 20180815\_20181107. The error bars represent 95% confidence interval.

Figure 11. The  $\Delta\phi_{another\_disp}$  inferred from Sporadic-E images on (a) 20160217\_20160525 and (b) 20090328\_20090628 reported by Furuya et al (2017).

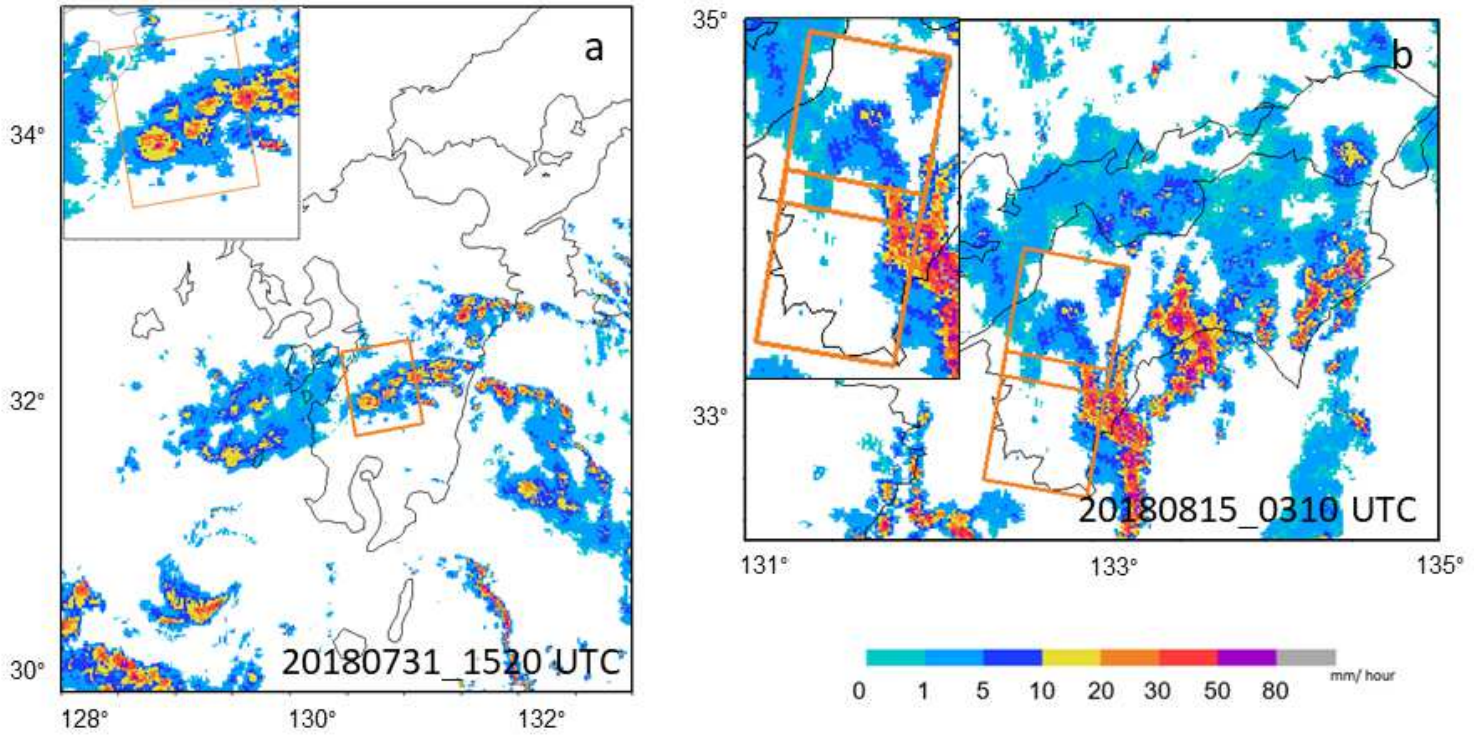
## Tables

Table 1. Details of InSAR data used in this study.

<b>Area</b>	<b>Dates (YYYYMMDD)</b>	<b>Path-frames</b>	<b>Original, high and low frequencies (GHz)</b>	<b>Split Bandwidth (MHz)</b>	<b>Perpendicular Baseline (Bperp)</b>
Kyushu	20180731-20180828 <sup>r</sup>	131-630	1.2575 ,1.2840,	15.867	41.1592 m
	20180410-20180828 <sup>f</sup>		1.2310		92.7221 m
Shikoku	20180815-20181107 <sup>r</sup>	22-2940, 2950	1.2575, 1.2840,		-274.9842 m
	20180228-20181107 <sup>f</sup>		1.2310		-337.8612 m

r: heavy rain, f: fair-weather.

# Figures



**Figure 1**

See Manuscript file for figure caption

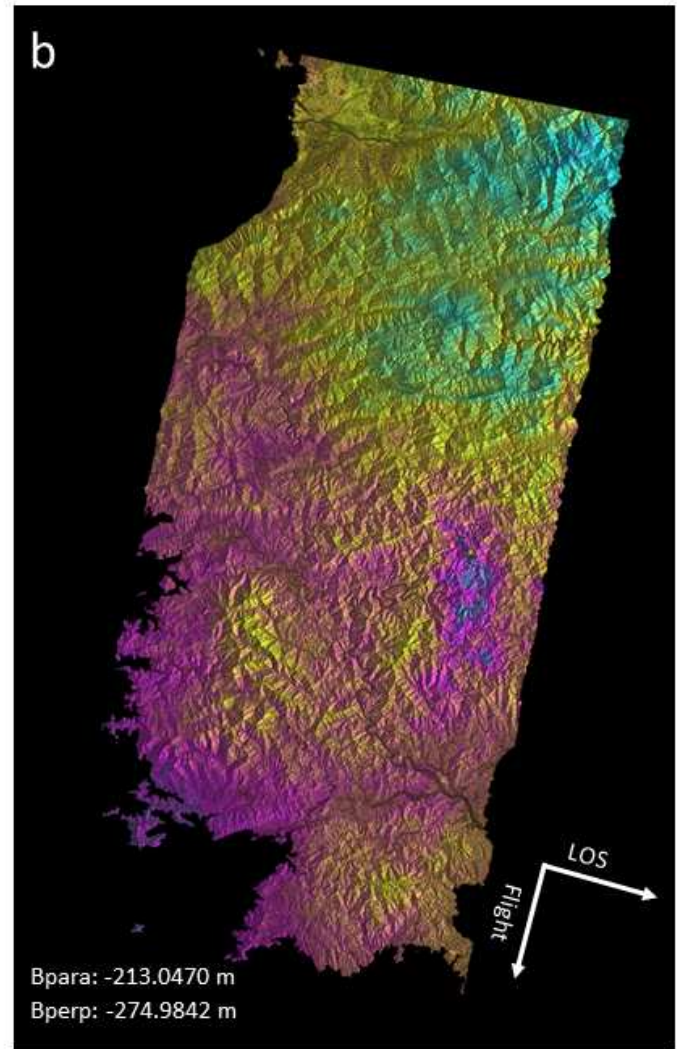
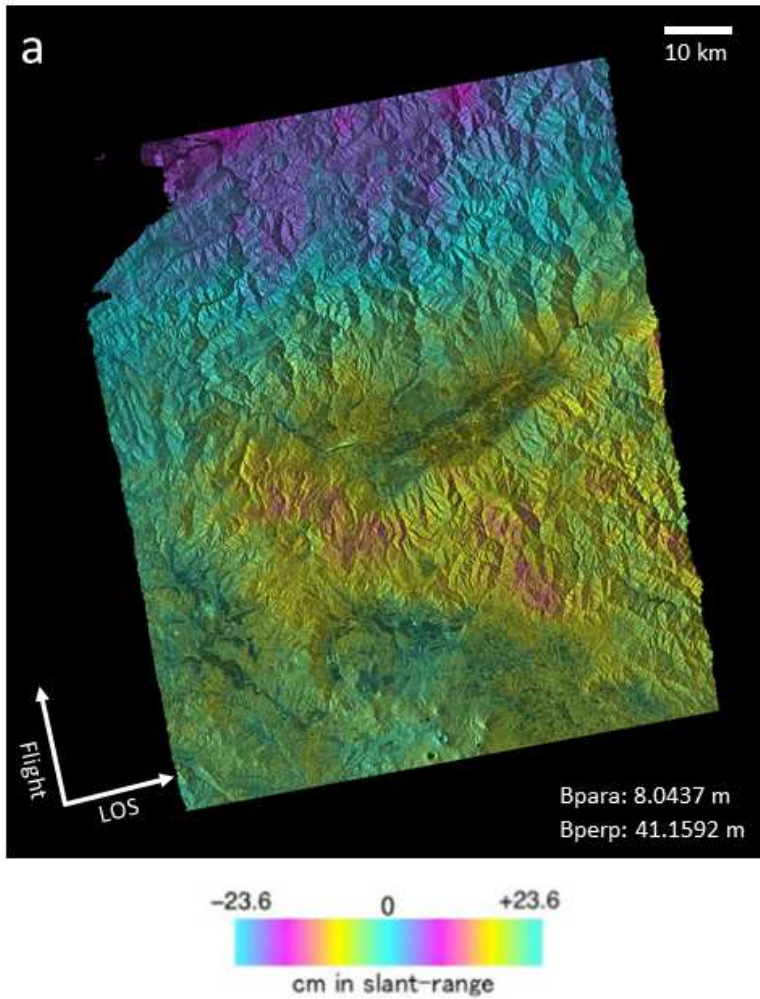


Figure 2

See Manuscript file for figure caption

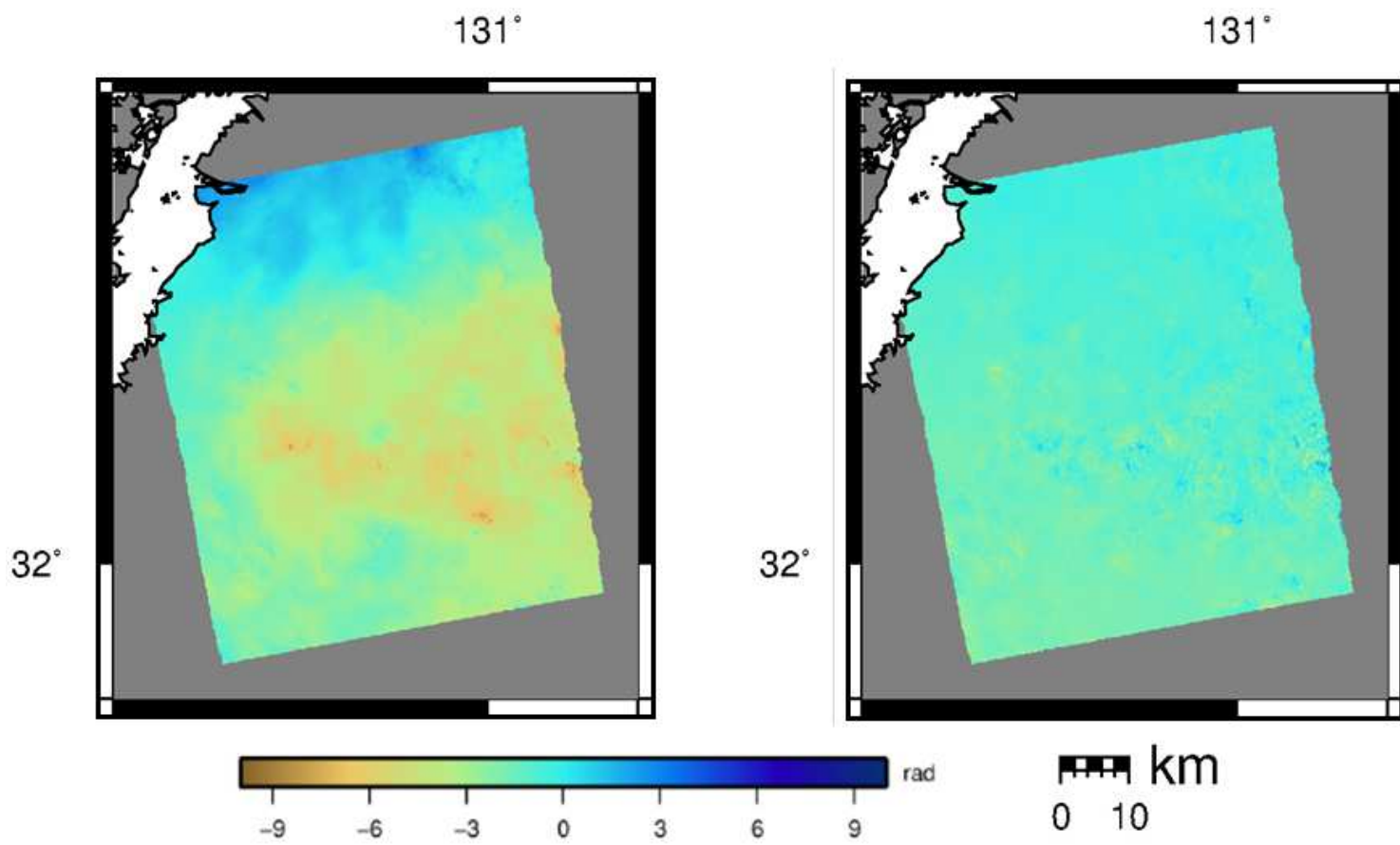


Figure 3

See Manuscript file for figure caption

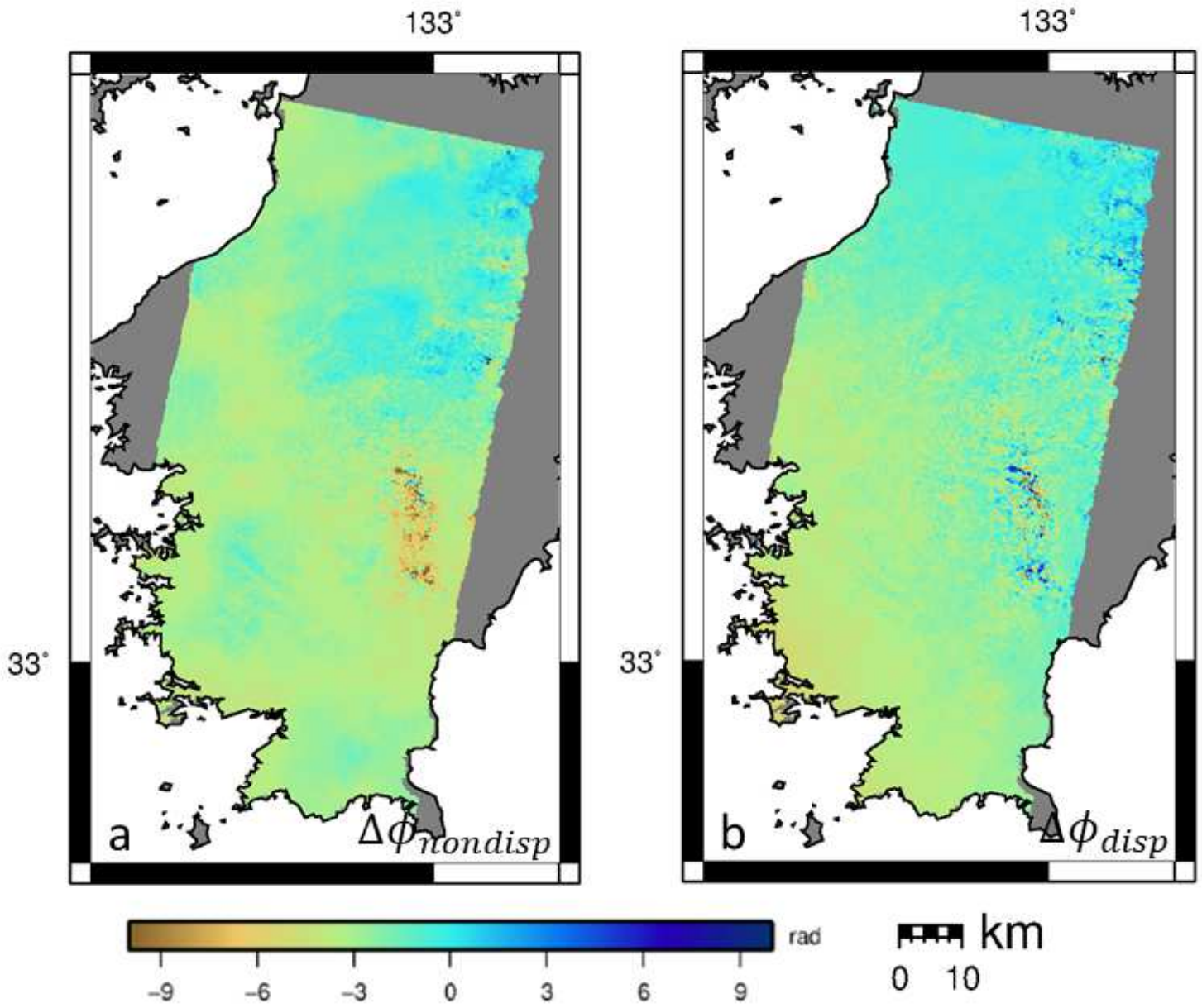


Figure 4

See Manuscript file for figure caption

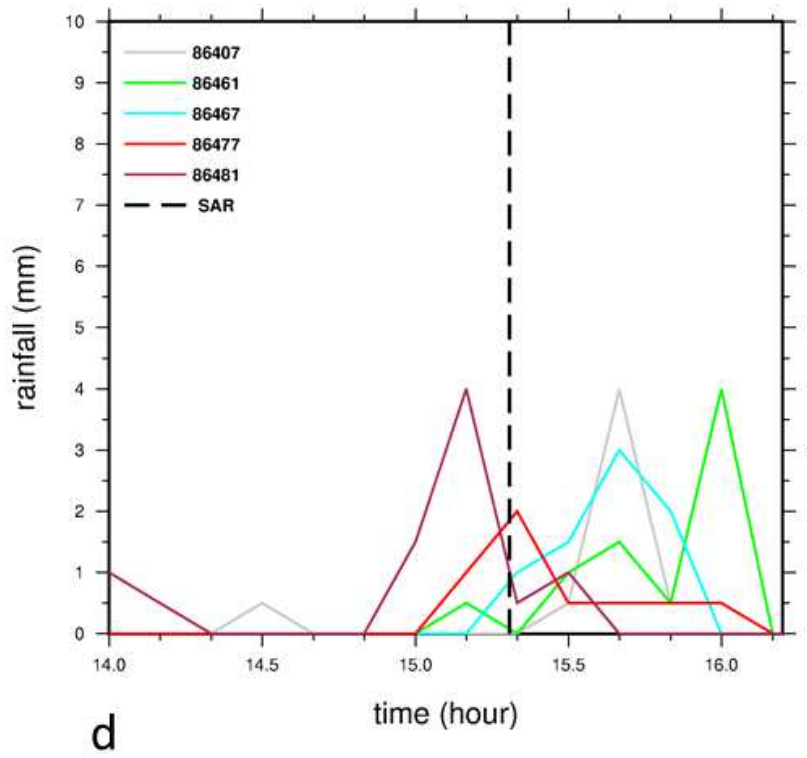
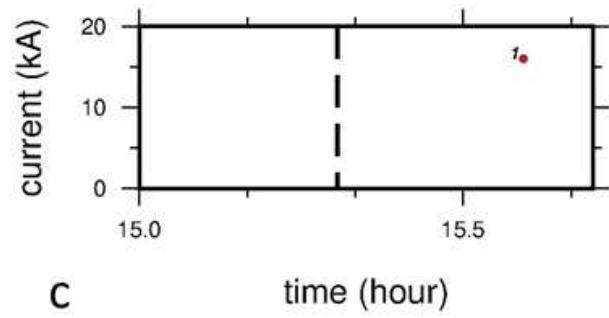
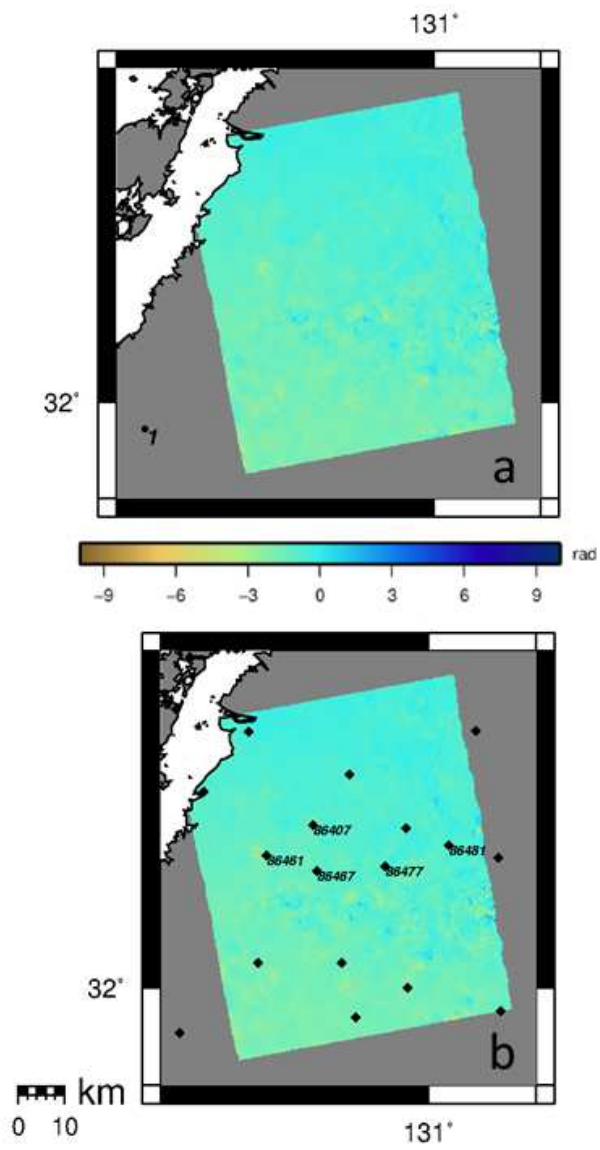


Figure 5

See Manuscript file for figure caption

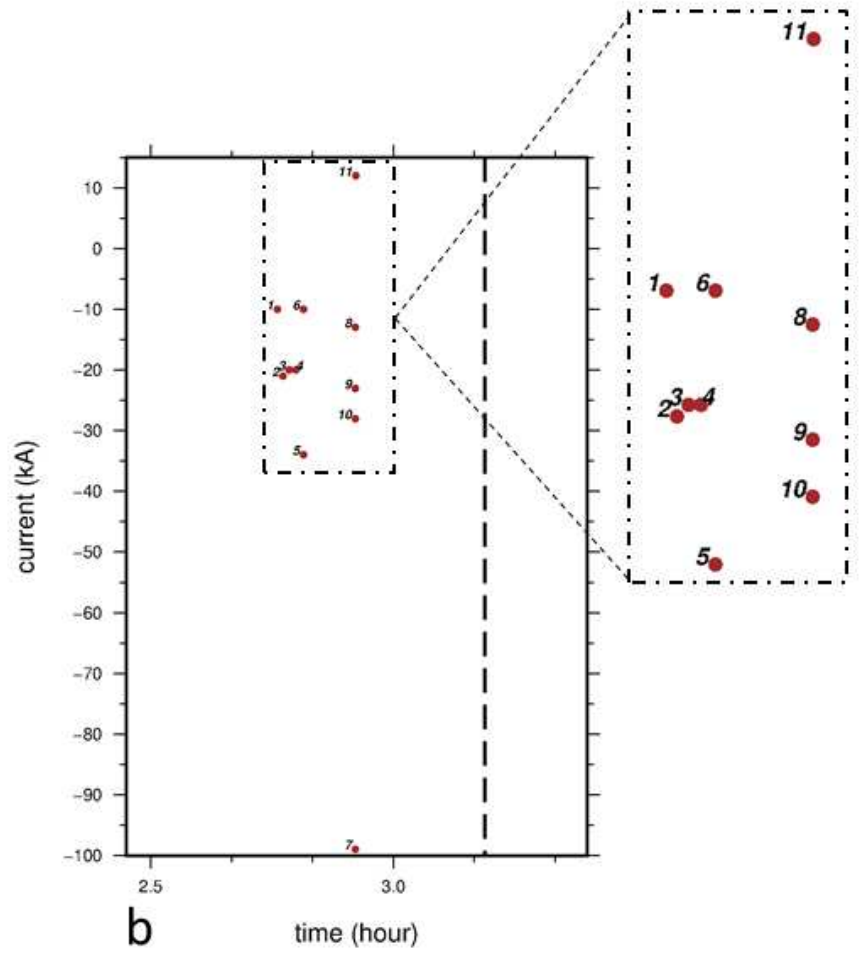
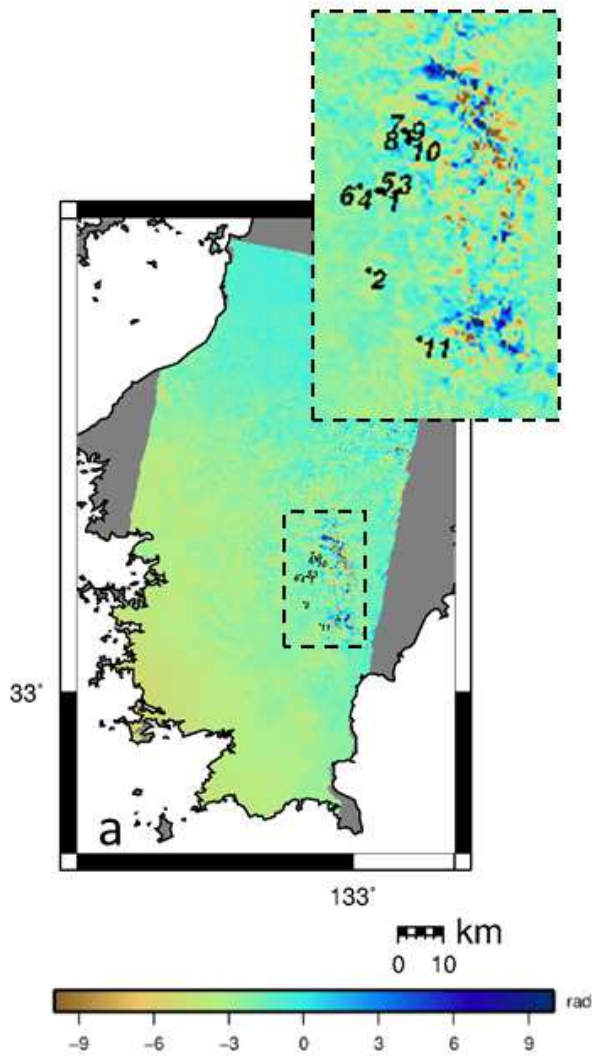


Figure 6

See Manuscript file for figure caption

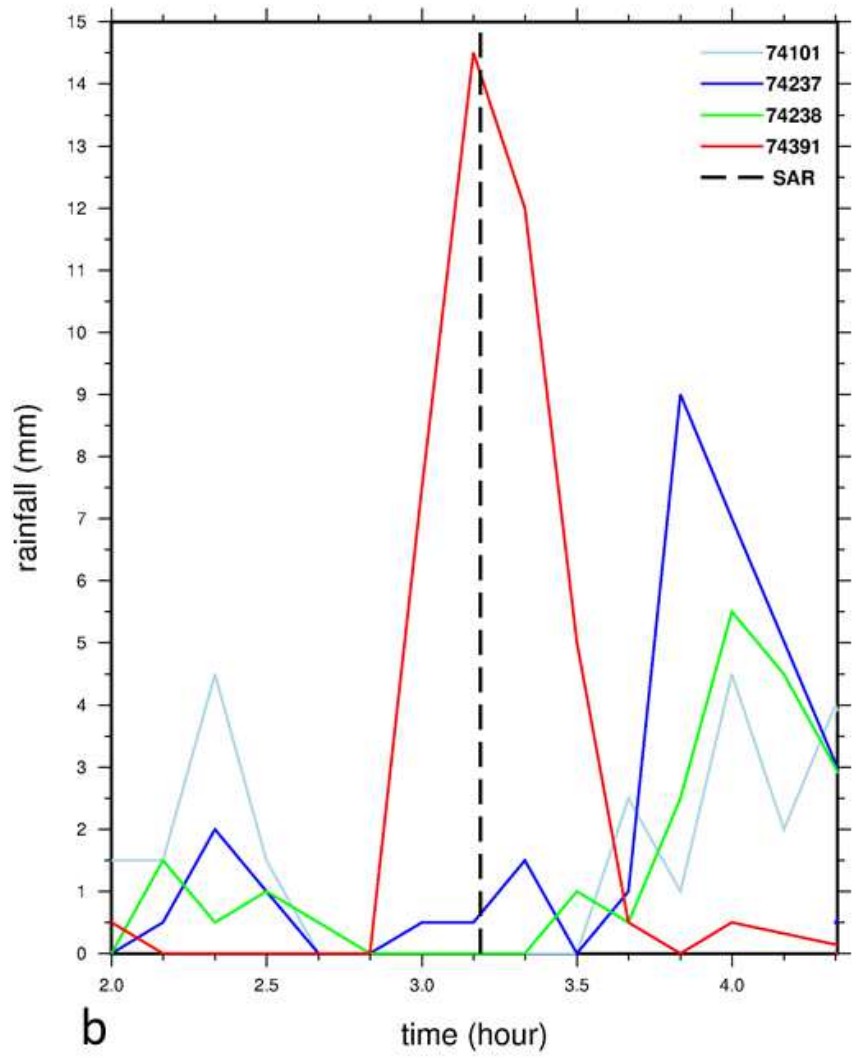
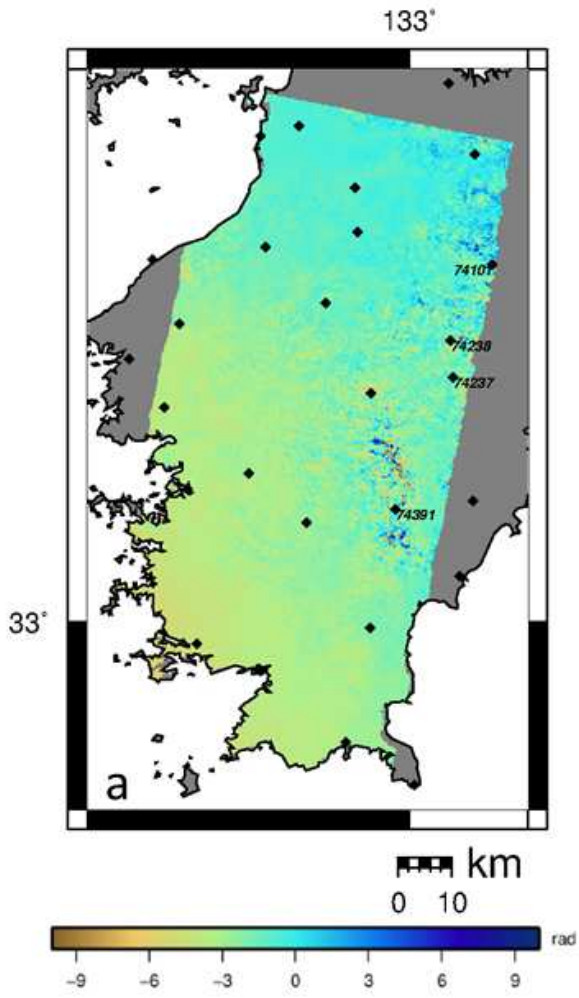


Figure 7

See Manuscript file for figure caption

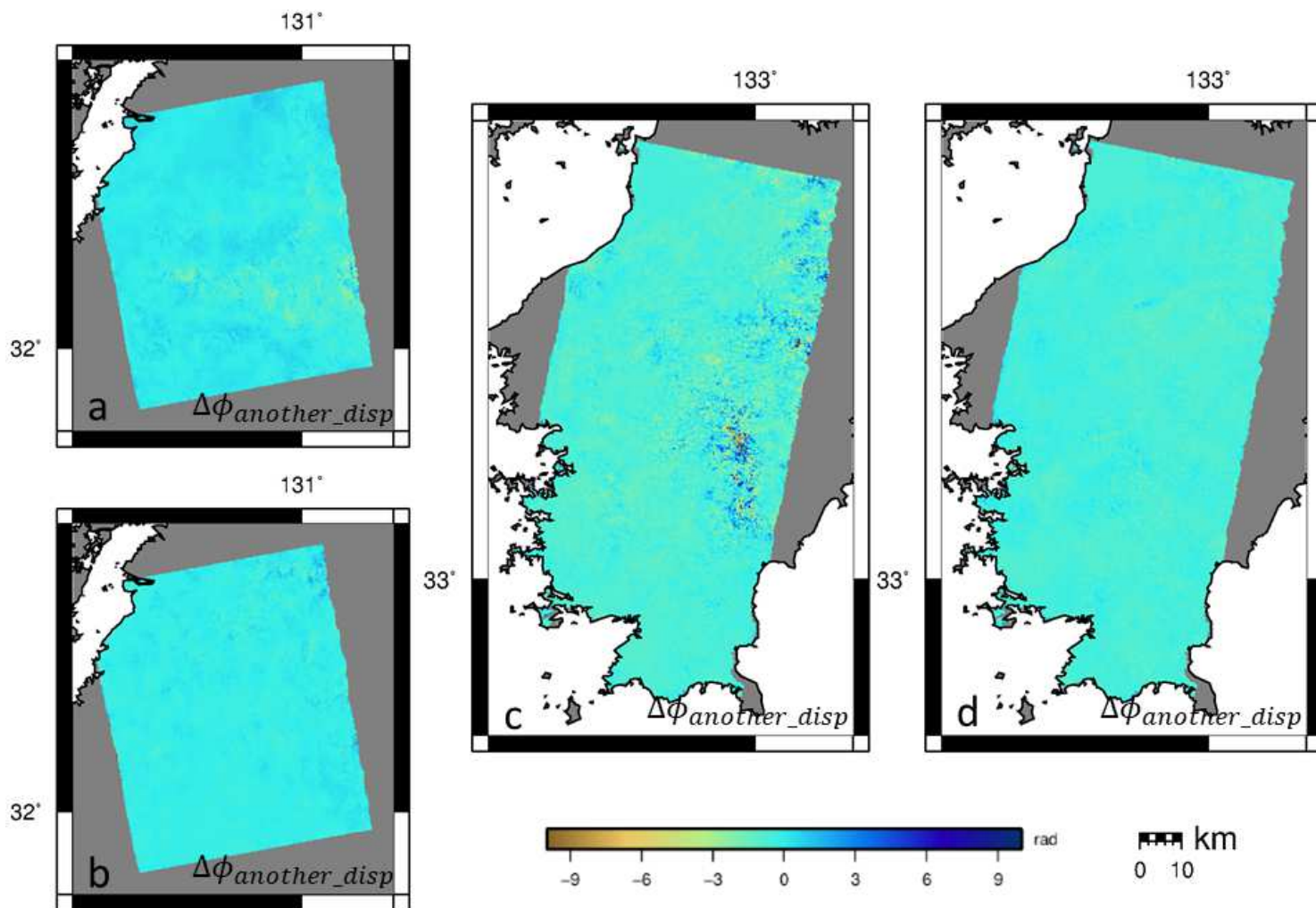
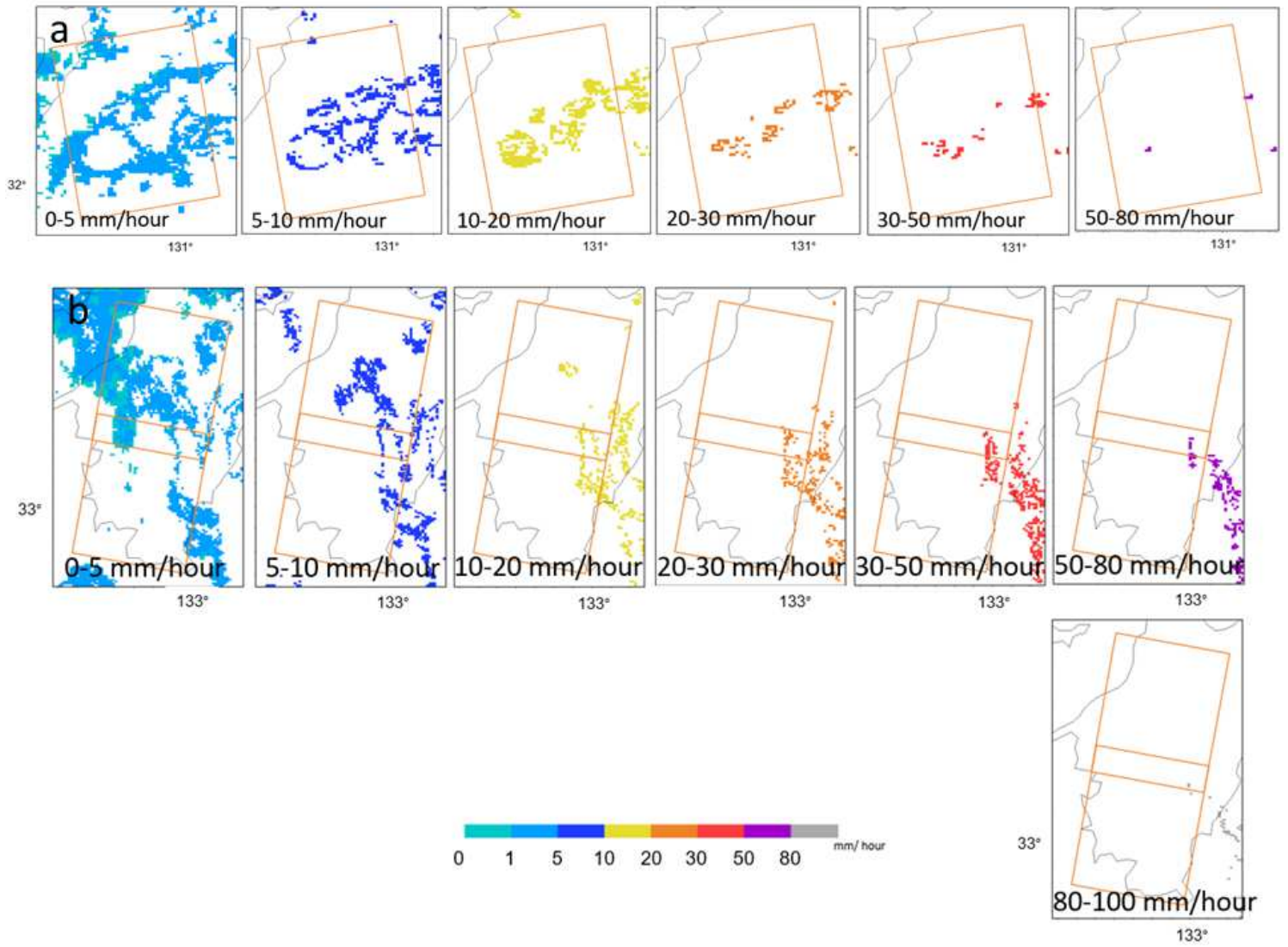


Figure 8

See Manuscript file for figure caption



**Figure 9**

See Manuscript file for figure caption

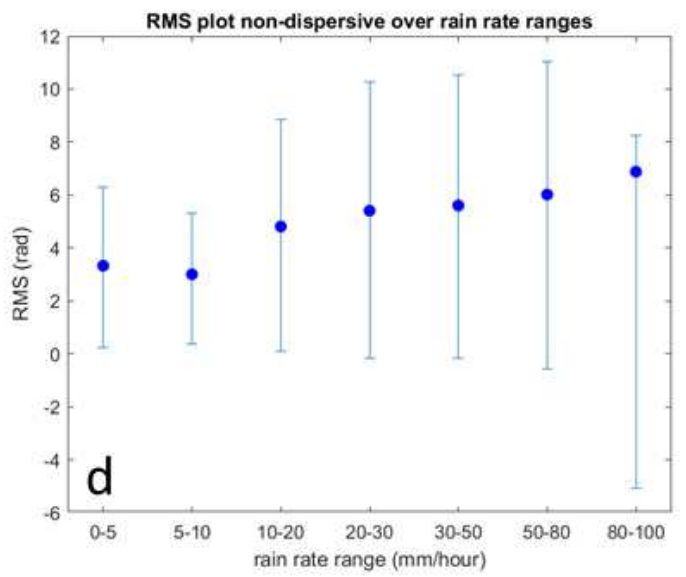
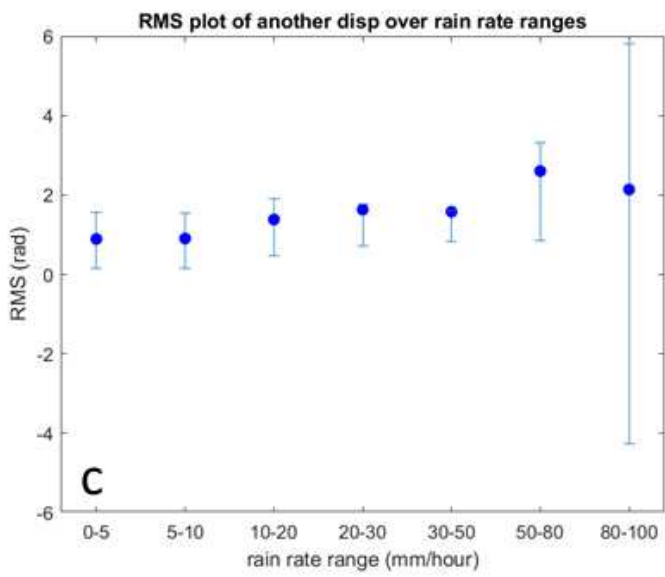
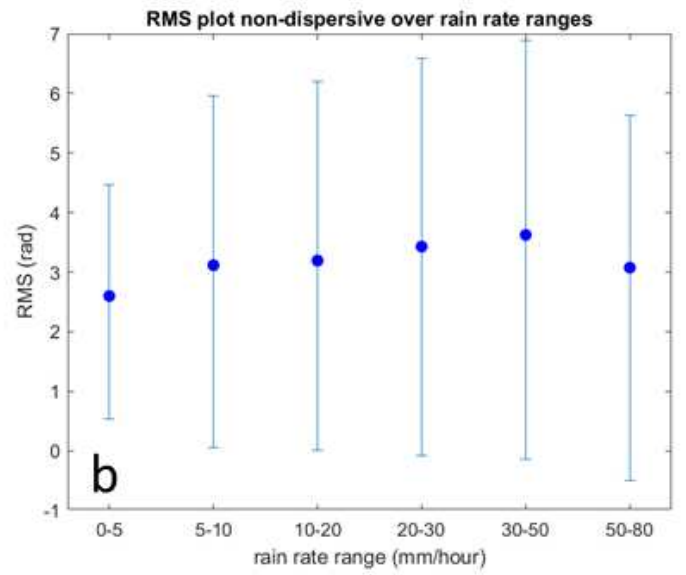
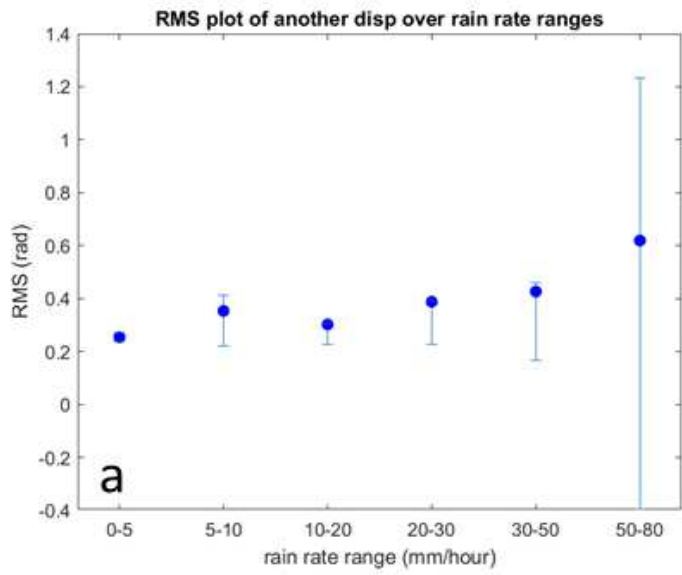


**Figure 10**

See Manuscript file for figure caption

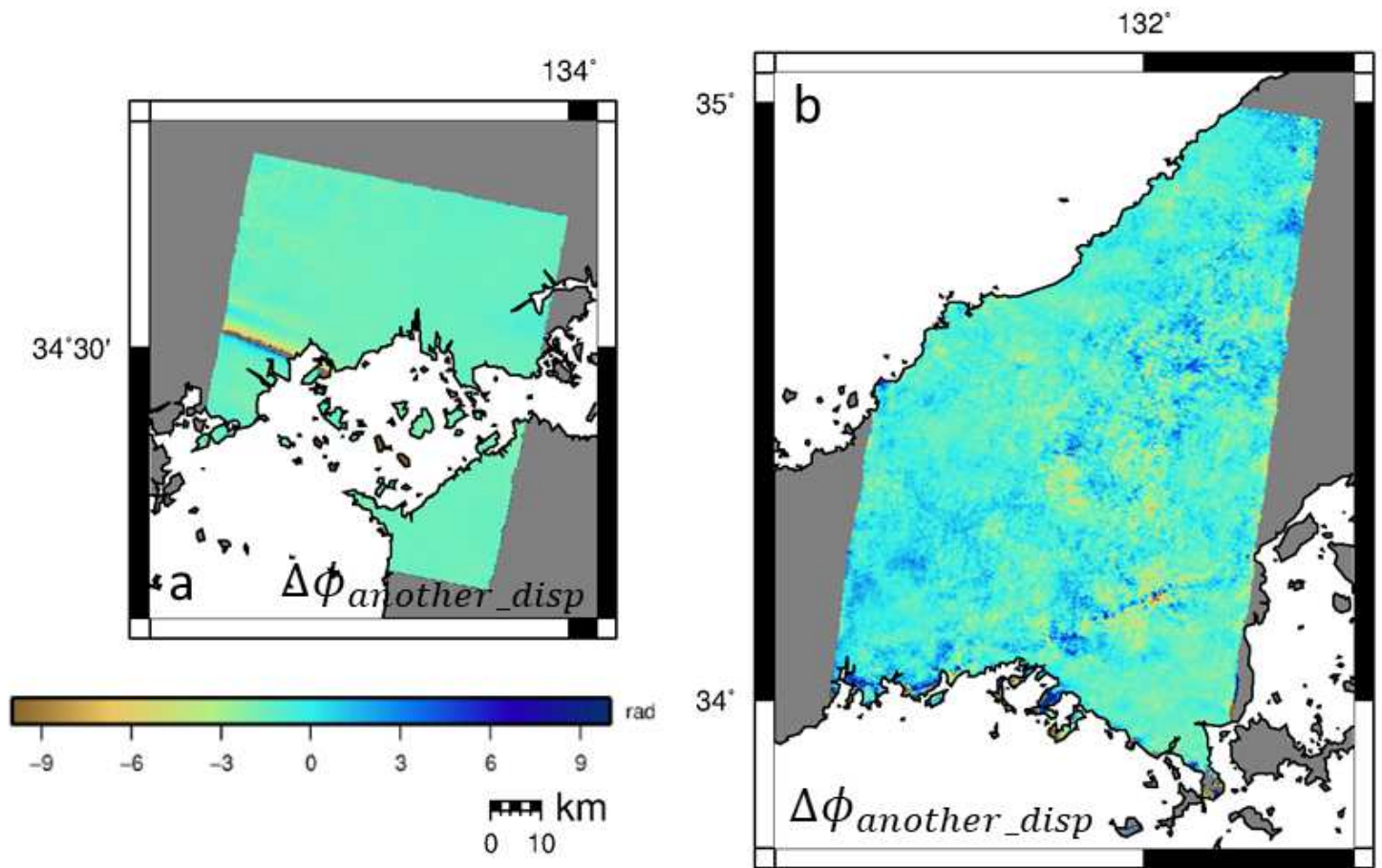


Figure 11

See Manuscript file for figure caption

## Supplementary Files

This is a list of supplementary files associated with this preprint. Click to download.

- [Supplementaryfile.docx](#)
- [graphicalabstract.png](#)